Batteries & Supercaps

Research Article
doi.org/10.1002/batt.202300202

Chemistry Europe
European Chemical Societies Publishing

www.batteries-supercaps.org

Extrusion 3D Printing of Patterned Cu Current Collectors for Advanced Lithium Metal Anodes

Daniele Callegari,[a] Lorenzo Airoldi,[b] Riccardo Brucculeri,[b] Umberto Anselmi Tamburini,[a] and Eliana Quartarone*[a]

Lithium (Li) metal is the most attractive anode material for the next generation Li batteries. However, crucial open challenges still limit its applicability at large scale, such as the low coulombic efficiency, unstable electrodeposition, and dendrite propagation with severe safety concerns. One strategy to address these drawbacks is the rational design of innovative current collectors for the Li anode. Here, we report on a simple, low-cost, and easily scalable process based on Additive Manufacturing technology via extrusion 3D printing to produce Cu current collectors with different and tuneable patterned structures. The current collectors are characterized by means of X-ray diffractometry, electron microscopy, profilometry and galvanostatic cycling. We show that the three-dimensional network can significantly stabilize the electrodeposition of Li, thanks to an enhanced electroactive surface area that enables a better Li accommodation without uncontrollable dendrite growth. Contrary to the planar current collector, the Li anode supported by the 3D current collectors exhibits stable and low voltage hysteresis at different current densities and can run for at least 330 hours without short-circuiting. Moreover, the evaluation of Li@3DCu anode in a LiFePO$_4$-based full cell by galvanostatic cycling reveals excellent rate performances, achieving specific capacity exceeding 100 mAh g^{-1} at 1 C and coulombic efficiency higher than 99%. These results show that the material extrusion 3D printing approach is a versatile strategy to develop new and safer anodes with a long lifespan and reduced amount of Li metal.

Introduction

The climate change associated with greenhouse gas (GHG) emissions has reached dangerous levels in recent decades, resulting in significant global warming. To address and remedy such issues, the International Energy Agency (IEA) has presented a roadmap called the "Net-Zero Emissions by 2050 (NZE) Scenario", aimed at limiting the average global temperature increase to 1.5 °C through an accelerated transformation of the energy sector in different fields.[1] The study looks at the physical energy infrastructures in place today, including fuel supply, power generation, and end-users such as industry and transport. Furthermore, considering that more than 60% of greenhouse gas emissions regarding transport mode are specifically attributable to road transport, a critical approach for the zero-emission goal is the transition towards e-mobility.

[a] Dr. D. Callegari, Prof. U. Anselmi Tamburini, Prof. E. Quartarone
Department of Chemistry, University of Pavia, Pavia, Via Taramelli 12, 27100 Pavia, Italy
and
National Interuniversity Consortium of Materials Science and Technology (INSTM) and GISEL, Via Giusti 9, 50121 Florence, Italy
E-mail: eliana.quartarone@unipv.it

[b] Dr. L. Airoldi, Dr. R. Brucculeri
Department of Civil Engineering and Architecture, University of Pavia, Via Ferrata, 27100 Pavia, Italy

Lithium-ion batteries (LIBs) are considered as the key-enabling technology as energy storage systems for electric vehicles. However, after huge progress in the performances of such devices, the theoretical limit of the energy density has been achieved, which is insufficient to meet the ever more stringent requirements in terms of power and energy density, safety, cost-effectiveness, and durability of the emerging technologies.[2]

The state-of-the-art LIBs have one obvious limitation related to the theoretical specific capacity of the anode material (i.e., graphite), which is 372 mAh g^{-1}. Over the years, numerous anodic materials, such as silicon, phosphorus, and nanosized transition metal oxides,[3,4] have been intensely investigated to increase the effective energy density of LIBs. However, despite the higher capacity delivered, especially in the case of Si-based systems, critical concerns, such as severe and irreversible structural modification, still limit their large-scale applications.

Lithium metal is another excellent alternative as an anode for Li batteries due to its very high theoretical specific capacity (3860 mAh g^{-1}), lowest reduction potential, and low density (0.534 g cm^{-3}), resulting in a very high energy density that makes it as the target anode for the next generation Li batteries. However, lithium metal is not exempt from crucial issues, as the unstable electrodeposition usually leads to dead Li and dendrites nucleation and proliferation. The dendrite formation upon cycling usually induces extended solid electrolyte interface (SEI) fractures that favour separator penetration. This phenomenon results in significant and dangerous short-circuit events, which seriously affect the safety of the storage device.[5,6]

One of the most promising strategies to face such challenges is enhancing the anode surface area and/or porosity. Indeed, according to Sand's law, the time of the dendrite nucleation is inversely proportional to the square current density of the anode surface. As a result, the Li anode surface area increase can significantly stabilize the metal stripping and plating upon charging/discharging and consequently hinder the proliferation of the metal dendrites.[7]

Many strategies have been adopted to improve the performances of the Li metal anode, such as metal surface protection, additives to stabilize the SEI, electrolyte engineering, and the design of three-dimensional current collectors.[8–10]

Due to the low resistivity and high electrochemical stability below 3 V, the anode current collector in Li metal batteries (LMB) is copper, used as a thin foil. The current collector properties have a great influence on cell performance. It has been shown that the tuning of Cu morphological features (e.g., porosity degree and the internal surface area) plays a role in the lithiophobicity, affecting the metal electrodeposition processes. In the case of a porous Cu current collector, for instance, the interconnected voids of the Cu skeleton favour the accommodation of Li deposition, resulting in increased coulombic efficiency and inhibited dendrite growth.[11]

Several studies report on enhancing the Cu current collectors surface area by fabricating 3DCu frameworks, enabling faster electron transfer, more ion absorption, and a reduction of polarization voltage of the Li stripping and plating processes. Such frameworks were usually obtained via chemical dealloying processes or copper micro-channels structures.[12–14] However, these methods involve expensive multi-step processes using potentially harmful etching reagents, which are unsuitable for a possible industrial scale-up.[15,16]

3D printing or additive manufacturing has recently gained considerable attention as an innovative tool to build up complex objects with well-defined and tuneable geometry using reduced amounts of materials. This technology has also been applied in the manufacturing processes for electrochemical energy storage, including batteries, especially for fabricating thick electrodes.[17–19]

The direct ink writing approach was explored to fabricate 3D-printed self-standing Copper frameworks with tuneable shapes, starting from the deposition of copper water-based colloids, followed by post-processing thermal treatments. The resulting 3D current collectors provided an enhanced surface area leading to low local current densities and an increased number of sites for lithium nucleation. Promising electrochemical performances were observed in terms of durable Li electrodeposition with low overpotential, high coulombic efficiency, and good capacity performances in full LiFePO$_4$-based cells.[20]

This study uses a material extrusion (MEX) approach to fabricate 3DCu current collectors (CC) for Li Metal anode batteries with different patterns and shapes. This method is well suited for the current collectors' fabrication since it allows layer-by-layer deposition of metals or metal oxides from pastes or highly loaded colloidal slurries, containing at least 88% of a powder dispersed in a solvent (usually water) and few amounts of organics (e.g., polymers). The proposed technique has many advantages over other AM methods, including significantly lower cost and higher versatility in terms of printable materials and complex geometry, high resolution depending on the needle size, and high printing speed. The investigated current collectors were printed directly from metallic powders and CuO-based pastes. Li metal was electrochemically deposited onto the differently shaped 3D CCs and the planar system to evaluate the pattern role in the electrochemistry of the Li metal anode. A full cell was ultimately assembled by using LiFePO$_4$ as a cathode to investigate the functional performance of the Li metal anode cell.

Results and Discussion

3D Cu current collectors: surface topography characterization

Figure 1(a) shows the image of a 3DCu current collector obtained by printing CuO-based inks and subsequent reduction via thermal treatment in the H$_2$/Ar atmosphere. Different patterns were easily explored; however, the reduction process was significantly detrimental in terms of overall patterning quality, especially reproducibility, and uniformity. This is due to the uncontrolled volumetric shrinkage during the reducing step that leads to the fracturing of the printed collector.

For this reason, the printing of Cu-based pastes was preferred to manufacture three-dimensional current collectors with remarkably higher pattern resolution and better quality without device cracking. The Cu paste was first investigated to find the composition with the best rheological properties (e.g., viscoelasticity) necessary for an optimal extrusion process. Figure S1 reports the *G* moduli and viscosity measurements obtained for the water-based ink with 88 wt.% of metallic powder. The paste shows a strong non-Newtonian character and high viscosity at a low shear rate that decreases abruptly by increasing the shear rate. This is an index of a proper shear thinning behaviour necessary for the MEX, enabling an efficient ink flow through the needle by applying pressure. Moreover, the *G* values and the difference between *G'* and *G''* suggest that the ink has a rigid but elastic solid behaviour allowing shape retention while the shear is applied.

Three patterns (coils, triangles, and squares) were produced, labelled as P1, P3, and P4 samples. In addition, a planar current collector (P0 sample) was also printed for the sake of comparison (Figure 1b). The 3D systems were characterized by X-ray diffraction (XRD) and EDX spectroscopy. XRD confirms that as-printed current collectors were metallic copper, showing the characteristic peaks at 43.7°, 50.8° and 74.3° referred to the diffraction planes of cubic copper (111), (200) and (220), respectively (Figure 1c). EDX analysis shows the typical signals expected for copper and excludes the presence of any significant impurities, demonstrating the capability of the MEX technology to produce pure and reproducible complex structures.

All the printed current collectors were characterized from a topographic point of view to check each pattern's quality.
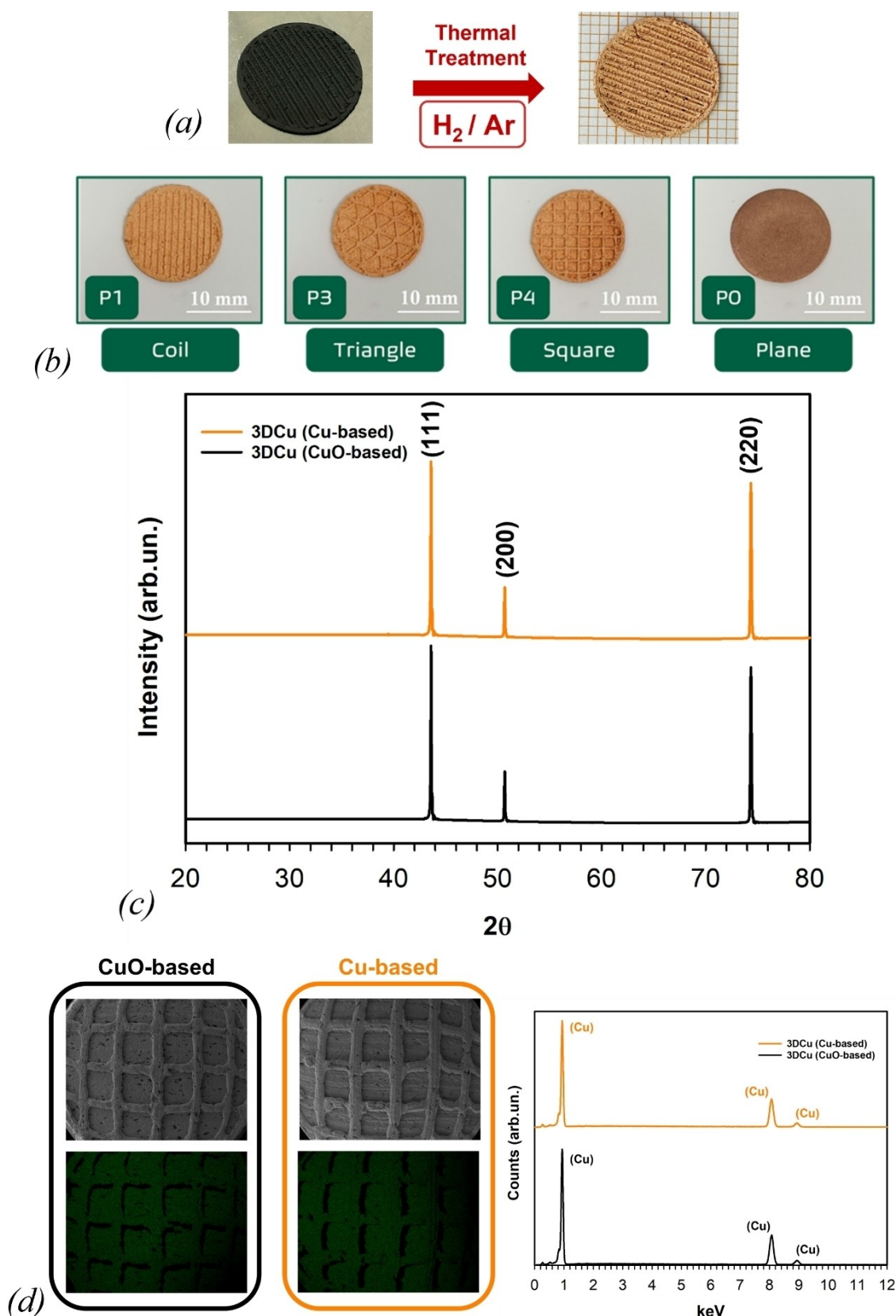
Figure 1. 3DCu current collectors produced by printing a) CuO- and b) Cu-based inks. c) XRD patterns and d) EDX/chemical mapping of the 3D collectors.

Batteries & Supercaps

Research Article
doi.org/10.1002/batt.202300202

Chemistry Europe
European Chemical
Societies Publishing

Figure 2 compares the 2D profilometry scans of the differently patterned P1, P3, P4, and P0 samples.

The profilometry analysis reveals an excellent pattern resolution regarding feature dimensions, heights, and shapes for all the geometries. As expected by the printing setup, the printed lines showed similar widths and heights of 450 ± 40 µm and 100 ± 15 µm, respectively, for each pattern. The roughness profiles, obtained from the profilometry scans and reported in Figure S2, point out a higher roughness for the P4 sample ($R_a = 14$ µm), whereas R_a values of about 9.0 µm and 8.0 µm are determined for the P1 and P3 current collector, respectively. An expected lower roughness ($R_a = 50$ nm) is in contrast obtained in the case of the planar current collected P0.

The roughness values were necessary to estimate the surface area of each current collector, which plays a crucial role in improving the electrochemical performance of the 3DCu-based anodes favouring a more stable Li electrodeposition, dendrite suppression, higher capacity, and power density.[21–24] The surface area of the current collectors was determined by calculating the geometrical area of the printed current collector and superimposing a 16-bit image collected by profilometry scanning to introduce the roughness features (Figure S3). The surface modelization was done using CAD software with complex 3D modeling tools (Rhinoceros 3D, Robert McNeel & Associates). The geometrical area was calculated as the sum of the areas occupied by the blue (printed lines) and red (inner layer) sections, respectively, as sketched in Figure 3(a–c) for the P4 sample and described in more detail in the Supporting Information.

The printed lines were assumed to be parallelepipeds with well-defined heights and width, as determined by the profilometry height profiles (Figure 3d–f). ImageJ software was, in contrast, used to measure the total length of the printed lines (about 167 ± 10 mm) from the images of the P1, P3, and P4 samples reported in Figure 1. Through this model combining the geometrical and morphological contributions, a multiplicator factor, R_s, is obtained from which an increment of the surface area of 100% is obtained for all the 3DCu samples with respect to the planar system with the same diameter.
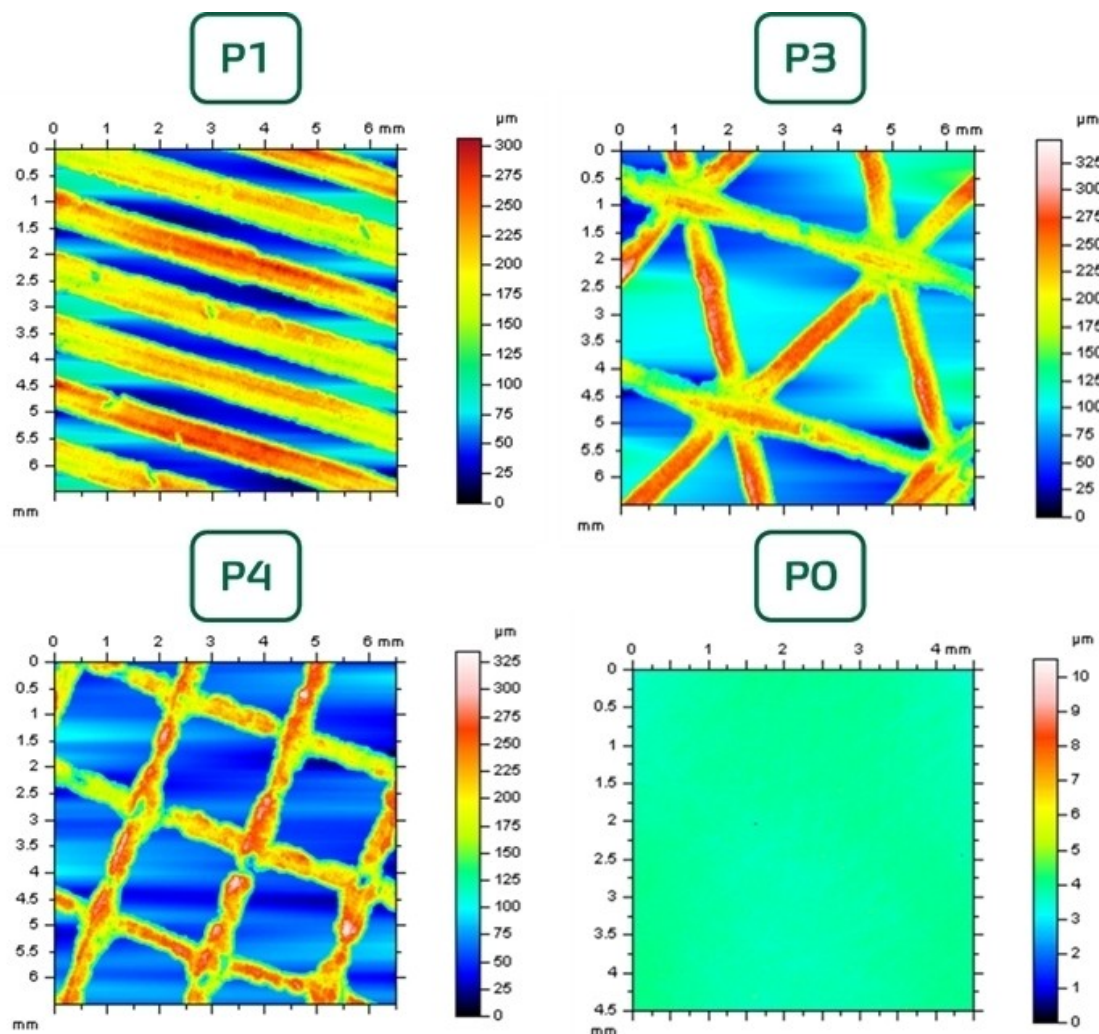

Figure 2. Profilometry 2D images of the printed 3DCu (P1, P3, P4) and plane (P0) current collectors.

Batteries & Supercaps

Research Article
doi.org/10.1002/batt.202300202

**Chemistry
Europe**

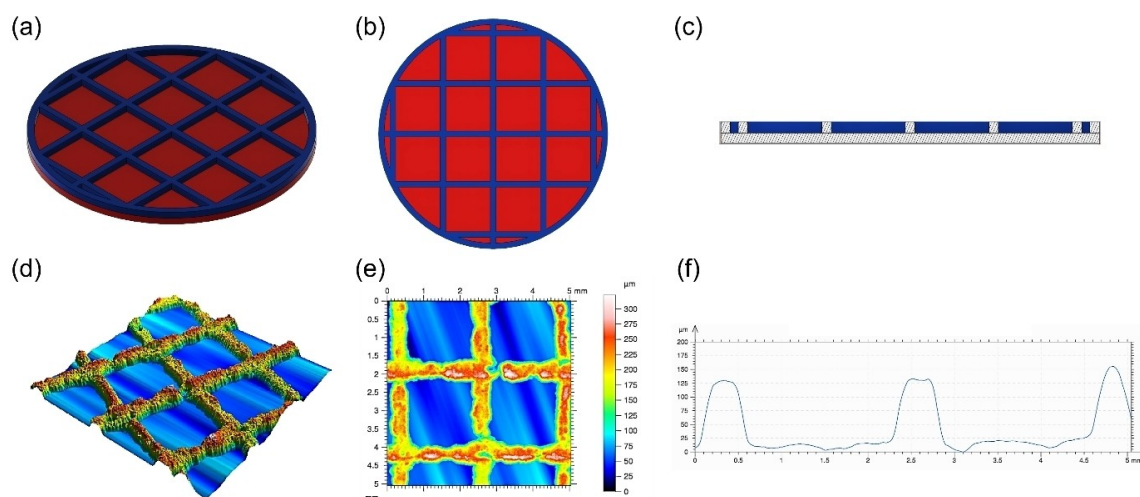European Chemical
Societies Publishing

Figure 3. Schematics of the 3D printed copper current collector (P4 sample). a, b) top view and c) cross-section view of the printed lines (blue) and the inner layer (red); d) 3D and e) 2D profilometry images of the P4 current collector; f) corresponding height profiles collected by the 2D profilometry scans.

Lithiation process of 3DCu current collectors

As mentioned, the 3D printed collectors were preliminary lithiated by electrochemical plating at a current density of $0.55\ mA\,cm^{-2}$ and an areal capacity of $10\ mAh\,cm^{-2}$. Figure 4(a) shows the Li typical plating voltage profile showing the deposition process characterized by a sharp potential drop that corresponds to the moment the lithium nucleation starts to take place on the 3DCu current collector. Subsequently, the potential slightly increases to reach a plateau of around 30 mV, indicating continuous lithium deposition.

The scheme reported in Figure 4(b) speculates on a possible Li plating mechanism. At the beginning of the process, Li metal particles nucleate preferentially on the top surface (dotted blue) along the entire printing lines and gradually cover the lines side sections and the inner layer (dotted red) of the 3D current collector. This phenomenon leads to a homogeneous and smooth Li deposition over the 3DCu samples, as noticeable in the SEM images of Figure 4(c). This result is in nice agreement with what is reported in the literature for three-dimensional systems printed by direct writing methods.[25] Moreover, the pristine 3DCu current collectors show large pores (Figure 4d) that can favor higher storage of liquid electrolytes and, consequently, a better-interconnected network for ionic diffusion.

The Li deposition onto the Cu current collectors was also investigated by quantifying the amount of metal plated over time in the 3DCu and planar Cu samples. Figure 5 compares the Li coating obtained at $0.55\ mA\,cm^{-2}$ and $10\ mAh\,cm^{-2}$ for the P4 and the planar P0 samples.

The Li deposition rate was determined by ICP-OES analysis after plating the P4 and P0 samples at different times (Tables S1 and S2). As the figure shows, the coating grows almost linearly with the plating time for the patterned current collector, achieving values ranging from ~2 to $15\ mg\,cm^{-2}$ (very close to the nominal ones) between 9 and 60 hours. In contrast, the plating voltage profile of the printed planar current collector (P0 sample) does not show any nucleation step (Figure S4), as confirmed by the corresponding Lithium loading, quantified by ICP analysis, that is remarkably smaller and does not increase with time. Such different behavior may be related to the topographic and morphological aspects of the current collectors. The higher surface roughness and area of the 3DCu sample favor the lithiophilicity of the current collector. A preferential Li-ion adsorption and an increased number of nucleation sites can be obtained thanks to rougher Cu surface. The porous structure can also induce the Li plating in the internal cavities providing a better metal accommodation and distribution along the current collector.[26] The result is an enhanced local current density that boosts the electron transfer process (expressed in terms of an increased exchange current density).[27] Additionally, the huge storage space provided by the 3D pattern can mitigate the typical volume deformation of the lithium anode that is responsible for cycling instability and severe cell failure. Similar improvements related to the porous framework have been also observed for other 3D printed networks, as, for example, in case of graphite-based skeletons for Li metal anodes.[28]

Electrochemical performance of Li@3DCu anodes

The Li stripping/plating processes of the Li@3DCu anodes were investigated by assembling symmetric cells whose working and counter electrodes were the printed systems (P1, P3, P4, and P0) and the Cu foil, respectively. The rate performance was tested by cycling all the investigated cells at different current densities, namely 0.5, 1, 2, 4 and, $8\ mA\,cm^{-2}$ (1 h for each half cycle). The resulting galvanostatic voltage curves are reported in Figure 6.

The Li@3DCu anodes show an overall ohmic behaviour in the full range of the explored current density. Especially in case of P4, the overpotential values increase nicely linearly with the current, as noticeable in Figure S5 that shows the V–I plots
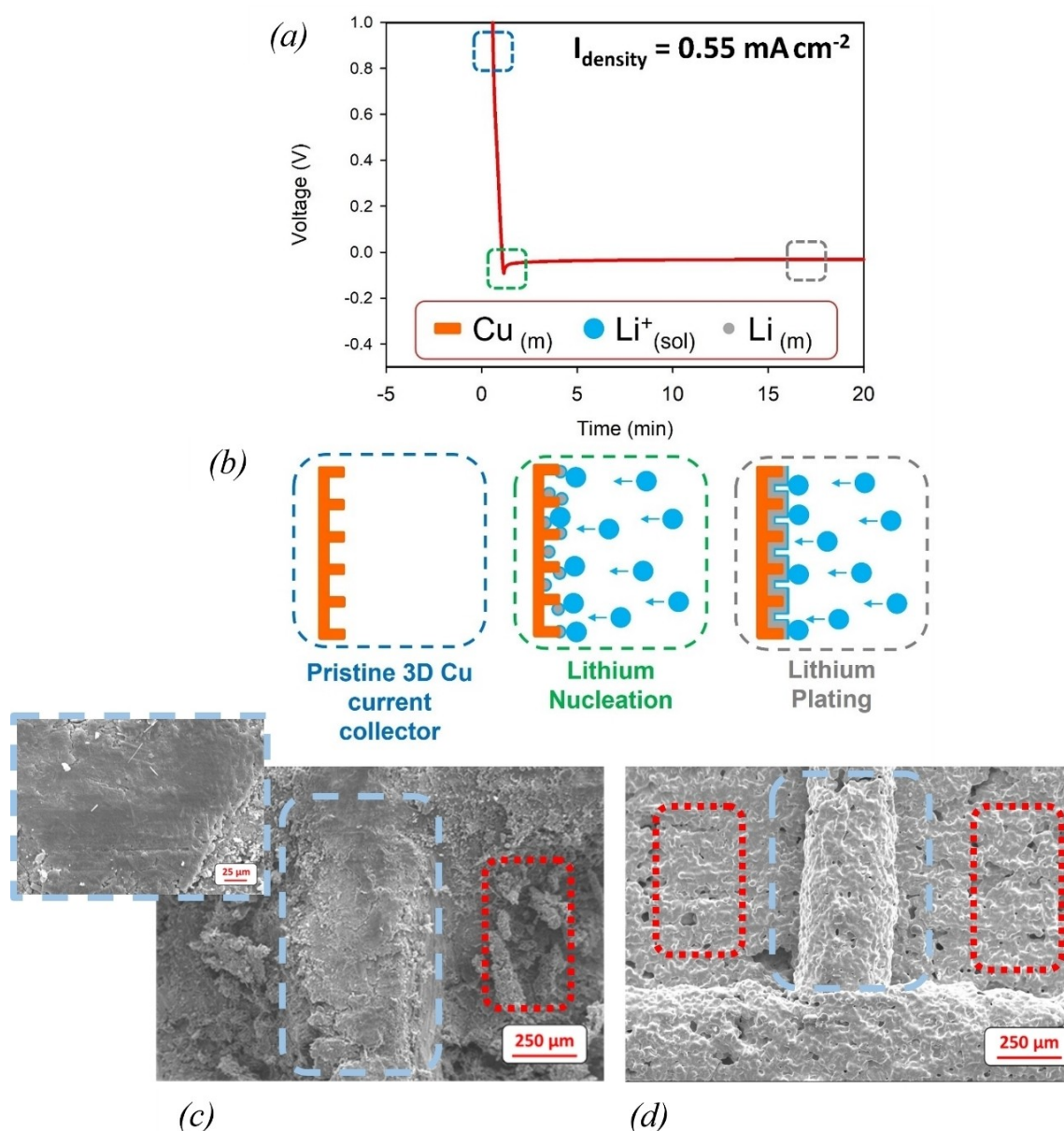
Figure 4. a) Galvanostatic profile of Lithium plating on 3DCu current collector at a current density of 0.55 mA cm^{-2} and b) naïve representation of lithium plating mechanics. SEM images of c) the 3D current collector after the plating process, Li@3DCu, (red dotted line: inner layer, light blue dashed line: top surface) and d) before plating (e.g. 3DCu sample)

collected for all the P samples (P0, P1, P3 and P4). In contrast, the planar current collector causes significant instability, especially during the initial galvanostatic cycles, when a remarkable deviation from the ohmic linear relationship is clearly evident. The Coulombic efficiency and cycling stability tests further demonstrate the beneficial effects of the 3DCu current collectors. Figure 7 reports the Li plating and stripping profiles of the Li@3DCu and Li@P0Cu anodes at 2 mA cm^{-2} (2 mAh cm^{-2}) over 300 hours after a Li deposition at 12 mAh cm^{-2}. For all the 3D current collectors, a stable voltage plateau is observed in the whole cycling period (see inset of Figure 7). The P4 anode shows excellent performances with more symmetrical profiles and lower overpotential ($<$ 20 mV)

that remains constant for all the cycles after the initial settling phase. Some variability in the coulombic efficiency are observed during the first cycles, especially in case of the planar P0 sample. This changeability has been frequently discussed in the literature for similar systems (see for example Refs. [20] and [25]) and can be related to the formation process of the SEI film. Indeed, during the first cycles of the metal electrodeposition, Li nucleation starts to take place, promoting the growth and stabilisation of the interface. Structural factors as tortuosity and inhomogeneity cab be responsible for the initial instability of the coulombic efficiencies.

Additionally, longer cycling stability is observed for the P4 anode in comparison to P1 and P3, likely related to the rougher
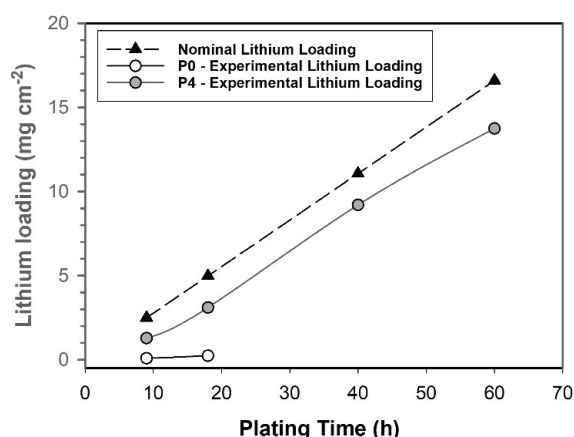
Batteries & Supercaps

Research Article
doi.org/10.1002/batt.202300202

Chemistry Europe
European Chemical
Societies Publishing

Figure 5. Quantification of lithium loading at different plating times on P4 and P0 Cu current collector.

may be related to the rapid growth of Li dendrite and the consequent penetration of the separator. Instead, the 3D architecture of current collectors with enhanced active surface area and roughness boosts the deposition of a larger amount of Lithium. As a result, it favours faster Li ion diffusion, stabilizing the metal electrodeposition through a decrease of the local current densities and a better distribution of the electric field. This hypothesis has been further consolidated in literature by ab-initio molecular dynamics, which indicated significantly lower nucleation energy barriers and consequently faster transport for Li ions for those substrates or current collectors which provided improved stripping and plating performances. Such lower activation energy for diffusion prevents gathering of ions and favours more homogeneous ionic flux, consequently hindering the generation of lithium dendrites.[26]

Average Coulombic efficiency higher than 95% is observed for all the investigated Li@3DCu anodes. The P4 sample shows stripping/plating efficiencies of about 100% for all the explored cycling ranges. In comparison, the P0 anode with a planar Cu current collector shows an unstable cycling behaviour with large fluctuation among the cycles.

The remarkably better functional performances of 3DCu (e.g., stable stripping/plating processes, small voltage hysteresis, a consistent voltage plateau, and high coulombic efficiency) are reasonably an index of a more efficient Li accommodation resulting in improved interfacial properties and enhanced
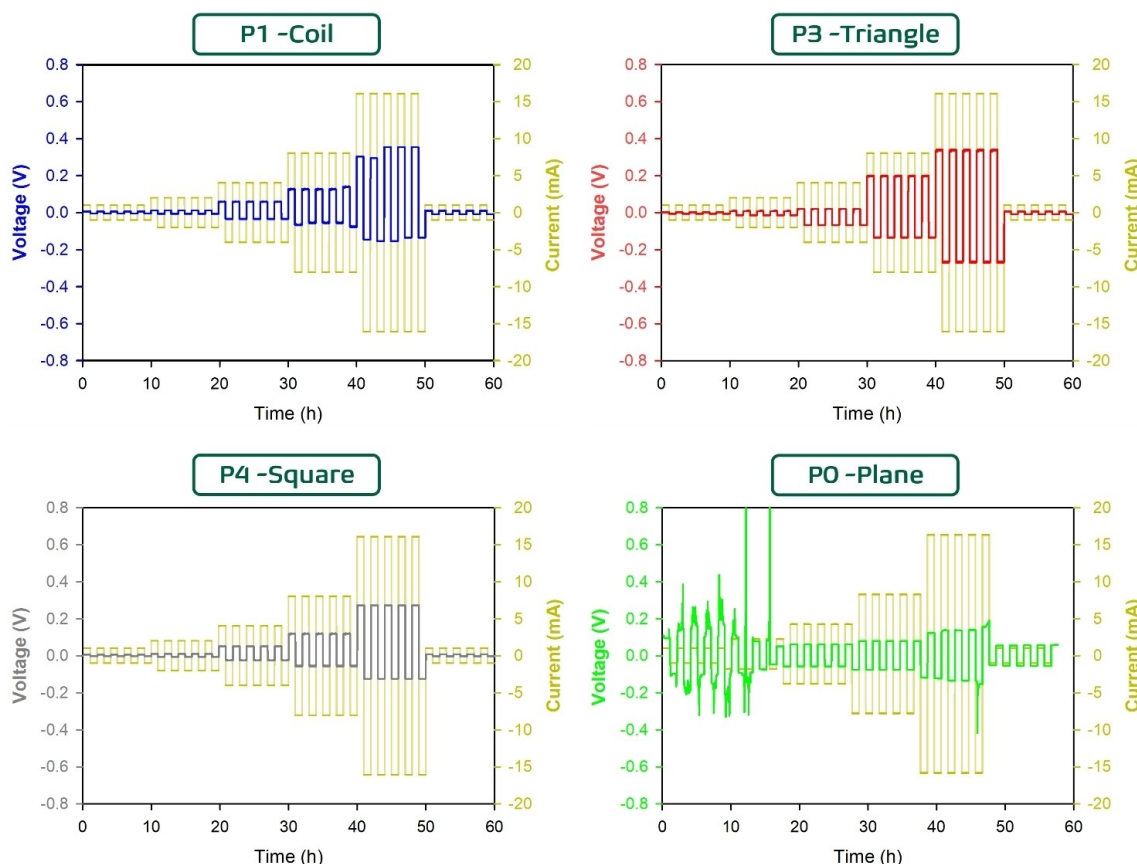
surface that could enable a larger electrolyte storage, delaying the battery drying up and preventing the electrode polarization. In contrast, remarkably unstable galvanostatic cycling is observed for the planar electrode (P0 sample), whose voltage profile is featured by intense voltage spikes, leading to a short circuit after only 15 cycles. The failure of the planar electrode

Figure 6. Rate performance of 3D (P1, P3, and P4) and plane (P0) current collectors with Li stripping/plating for 2 hours in each cycle.

Batteries & Supercaps

Research Article
doi.org/10.1002/batt.202300202

**Chemistry
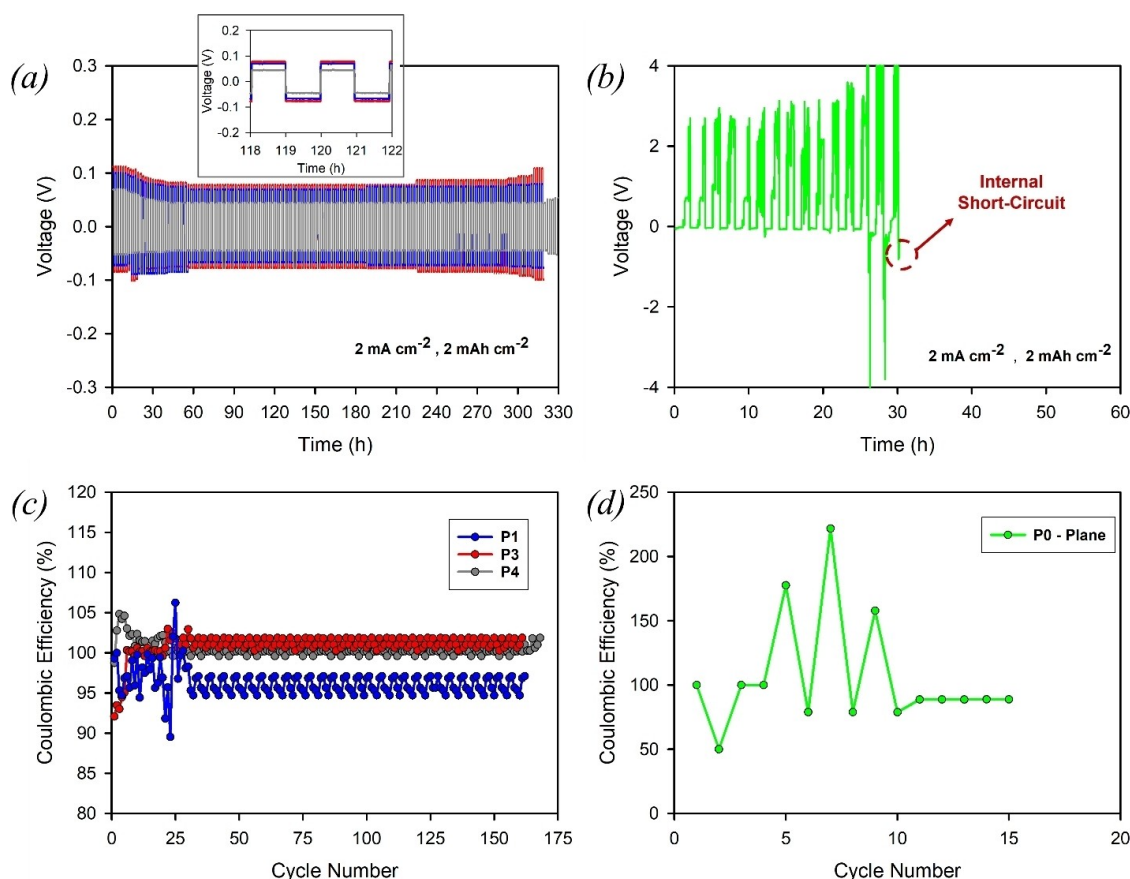Europe**

European Chemical
Societies Publishing

Figure 7. a) Galvanostatic cycling at 2 mA cm^{-2} of the Li@3DCu (P1, P3, and P4) and b) planar Li@Cu anodes with a stripping/plating capacity of 2 mAh cm^{-2}. The inset in (a) shows, as an example, the voltage profiles for the cycles range between cycle number of 59 and 61. c, d) Coulombic efficiency of the Li@3DCu (P1, P3 and P4 samples) and planar Li@Cu (P0) at 2 mA cm^{-2}.

kinetics of the charge transfer processes concerning the planar current collector. Similar beneficial effects in terms of dendrite suppression and improved electrochemical behaviour were observed in literature for LMBs with current collectors based on three-dimensional Cu networks, also with nanostructured design.[29]

The morphological evolution of the 3D current collectors due to the galvanostatic cycling was investigated for the best-performing system, namely the P4 sample. Figure 8 reports the SEM images of Li@3DCu after 330 hours of stripping and plating. The Li deposition is quite homogeneous, covering the whole Cu skeleton. No critical aggregates or asperities due to
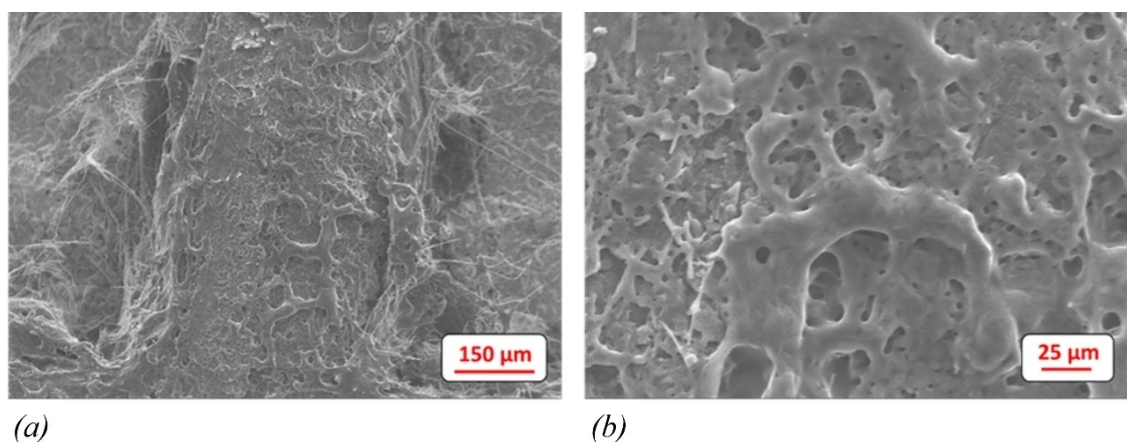

Figure 8. Surface SEM images of Li@3DCu (P4 current collector) after more than 300 hours of continuous stripping and plating.

Batteries & Supercaps

Research Article
doi.org/10.1002/batt.202300202

Chemistry
Europe
European Chemical
Societies Publishing

overgrowth phenomena that can lead to the formation of dendrites are evident. This result might suggest that the Li nucleation and growth occur in all directions without any preferential pathway, promoting a uniform Li-ion concentration and electric field distribution and favouring more stable metal electrodeposition.

Taking into account the promising performances of the P4 sample and in order to further explore the practical application of the 3DCu current collectors, full cells were assembled with LiFePO$_4$ as cathode and Li@3DCu (P4) as an anode, with two different Li loadings, namely 9 mg cm^{-2} (22 mAh cm^{-2}) and 13 mg cm^{-2} (33 mAh cm^{-2}). A standard full cell produced with Li tape onto a Cu metal foil as a current collector was also investigated as a baseline (Figure S6).

Figure S7 shows the Nyquist plots obtained by potentiostatic electrochemical impedance spectroscopy (PEIS) to evaluate the charge transfer resistance (R_{CT}) between the two investigated cells before and at the end of the rate capability test. Despite a higher R_{CT} value before cycling in the case of the Li@3DCu-based cell, equal charge transfer resistances are achieved during the galvanostatic cycling. Figure 9 reports the rate capability of the cells with 3D current collectors in the current range between 13 mA g^{-1} (0.08 C) and 170 mA g^{-1} (1 C). Overall, good and comparable performances are observed for both the investigated systems, especially at lower current densities, with coulombic efficiency close to the unit. In the particular case of the Li@3DCu anode with higher Li loading (13 mg cm^{-2}), higher capacities are also obtained at intermediate C rates (e.g., 100 mAh g^{-1} at 1 C), with rate capability performances pretty similar to the baseline cell, including bulky Li as the anode (Figure S6).

These encouraging results suggest that printing 3D current collectors, properly designed in terms of surface area and pattern geometry, is a promising strategy to produce well-performing and stable cells combining good interfacial properties, stable electrodeposition, and a significantly lower amount of Li.
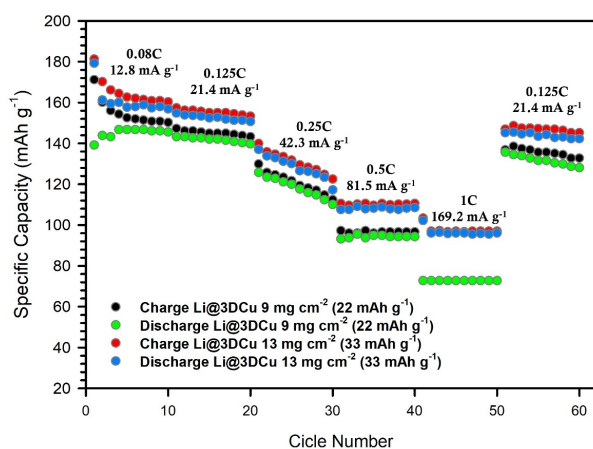

Figure 9. Rate performance comparison between full cells with different Li loadings, 9 mg cm^{-2} (22 mAh cm^{-2}) and 13 mg cm^{-2} (33 mAh cm^{-2}), at different current densities.

Conclusions

3DCu current collectors with different patterns (coil-like, triangular, and square) were successfully produced from high solid loading metallic powder via an additive manufacturing approach using an in-house modified extrusion 3D printer. The advantage of the material extrusion technology (MEX) is to print a 3D framework with significantly enhanced surface area and porous network capable of accommodating Li in higher concentration and more homogeneous distribution. The enhancement of the active surface area and roughness acts on the electric field's distribution and decreases the local current density to improve the metal electrodeposition behaviour and boost the formation of a more stable SEI. The result is the suppression of the Li dendrite propagation and the alleviation of the volume change. The more performing Li@3DCu anode was based on the square-patterned framework that exhibited a very good stripping/plating behaviour with a lifecycle of more than 330 hours at the areal capacity of 2 mAh cm^{-2} without cell drying up or short-circuiting. Coulombic efficiencies exceeding 99 % and low voltage hysteresis were achieved over the cycling test.

The extrusion-based printing strategy is a unique, simple, and easily scalable technology that can be employed in manufacturing innovative current collectors capable of solving safety problems and improving the electrochemical performances of the metal anodes in next-generation Li batteries and other rechargeable metal battery technologies.

Experimental Section

Inks preparation

The two types of inks were prepared by dispersing a defined amount of powders, namely 88 wt.% of metallic copper (Cu by New Linbraze) or 80 wt.% of copper oxide (CuO by VWR) in the proper quantity of a water solution containing 26 wt.% of a polymeric additive, that is polyethylene oxide *co*-polypropylene oxide-*co*-polyethylene oxide (Pluronic® F-127, Sigma Aldrich, MW 12600), necessary to control the system stability and rheology.

The copper powder consisted of spherical particles with particle diameter up to 50 µm. In comparison, copper oxide powders present a broader size distribution with agglomerates up to 100 µm as measured by SEM analysis (Figure S8). All inks were homogenized using a syringe-to-syringe mixing procedure developed in our previous study,[30] that consists of mixing all components directly in the extruder syringe (30 ml Nordson EFD) at temperatures below 10 °C. This approach avoids any loss of powder and solvent, allowing optimal printing reproducibility.

Printing apparatus

The current collector meshes have been realized using an in-house modified 3D printer from (*e3d* printer, ToolChanger & Motion System Bundle). SMC Corporation provided all the pneumatic components required to control the ink extrusion. They include three-port pilot-operated poppets (VP342R-5YO1-02FA), precise pressure regulators (IR2020-F02-A), high-precision digital pressure switches (ISE20-P-01-L), and high noise reduction silencers (ANB1-

Batteries & Supercaps

Research Article
doi.org/10.1002/batt.202300202

Chemistry Europe
European Chemical
Societies Publishing

02/03). In addition, a pressure relief three-port valve (VHS40-F04 A) and a filter regulator with a backflow function (AW40-F04*-B) were employed to stabilize the airflow inlet. The colloids were extruded at a pressure of 1.5 bar through conical needles, with an inner diameter of 0.4 mm (*Nordson* Optimum® SmoothFlow™). The open-source software *Ultimaker Cura Slicer* was chosen to set all the printing parameters, such as speed, extrusion width, infill density, and shape. The latter two parameters were used to create the different electrode patterns. Printed on a thin graphite sheet, the objects were dried in air to remove most of the water and then treated in a high-temperature furnace for the sintering step (see Figure 10).

The thermal treatment included three steps: de-binding, chemical reduction, and sintering. First, the de-binding was performed using a 1 °C min^{-1} ramp from room temperature to 300 °C under air. It was then followed by a chemical reduction step for 6 hours at 600 °C in Ar/10 % H$_2$ atmosphere. Finally, sintering was performed at 1050 °C for 6 h in the same reducing environment.

Characterization

Rheology measurements of the printed copper paste were performed on a rotational rheometer (MCR 102, Anton Paar, I) at 25 °C in a plate-plate configuration (PP20 mm diameter) with a set gap of 1.5 mm. Sample viscosity was measured at increasing shear rates between 10 and 1000 s^{-1} to assess the effect of copper powder addition on viscosity compared to pure water-based Pluronic® gel.

Dynamic oscillatory measurements assessed sample viscoelasticity. In the stress sweep test, increasing stresses were applied at a constant frequency (1 Hz). The elastic response of the sample, expressed as elastic (G') and loss (G'') modulus, was measured. In the oscillation test, a shear stress, chosen in the linear viscoelastic region previously determined, was applied at increasing frequencies (1 to 10 Hz) and G' and G'' profiles were recorded.

A stylus profilometer (AP06 KLA Tencor), equipped with a standard silicon tip (radius 2 μm), measured surface topography and sample roughness. A force of 0.50 mg was imposed on the silicon tip. Root mean square roughness values and 3D images were obtained by the instrument Apex software. For each analyzed sample, scans of 6.5 mm×6.5 mm and 4.5 mm×4.5 mm were performed for 3D and plane current collectors, respectively. The measurement has been carried out with a scan sampling rate of 20 Hz.

X-ray powder diffraction (XRPD) analyses were conducted using a Bruker D2 PHASER 2nd Gen X-ray diffractometer in the 2θ range 20°–80° (step size 0.024°), with Cu K_α radiation. The morphological and compositional characterization of the samples were performed using a Tescan Mira3XMU microscope operated at 20 kV equipped with EDAX EDS analysis system.

ICP-OES was performed by a Thermo Scientific CAP 7400 Duo, equipped with a quartz torch, a charge injection detector, and a Cetac ASX-560 autosampler. The Li quantification was carried out in HNO$_3$-digested solutions in the axial mode, with a LOD of 100 ppb and 670.78 nm as wavelength, by an external standard calibration curve. ICP grade standards 1000 mg L^{-1} (Merck) were diluted to 1–5–10 mg L^{-1} and then acidified to a final concentration of 1 % nitric acid (from ultrapure 65 % HNO$_3$, Merck). The measurements conditions were as in the following: nebulization gas flow: 0.5 L min^{-1}; power RF: 1150 W; cooling gas flow: 12 L min^{-1}; auxiliary gas flow: 0.5 L min^{-1}; peristaltic pump speed: 50 rpm; frequency: 500 Hz; intake flow: 1.5 L min^{-1}.

The functional performance of Li@3DCu anodes (i.e., galvanostatic stripping/plating experiments and rate performance) was investigated by assembling Li|Electrolyte|Li@3DCu symmetric 2032-type coin cells in Ar-filled glove box (H$_2$O and O$_2 < 0.5$ ppm). Cells including Li metal foil as anode were assembled and tested for comparison. The employed electrolyte was 1 M lithium bis(fluorosulfonyl)imide (LiFSI) in EC:DMC (50:50 vol.%) supported by a Celgard 2500 separator. Before each electrochemical test, the printed current collectors were lithiated by plating experiments in a current density range between 10 and 40 mAh cm^{-2}.

The anode rate performances were performed using a battery tester (Arbin, model BT-2000) by galvanostatic cycling at current densities ranging between 0.5 and 8 mA cm^{-2} (1 hour/half-cycle). The anode stability tests were performed by galvanostatic cycling at 2 mA cm^{-2}. Full cells were finally assembled using Li@3DCu as the anode and LiFePO$_4$ as the cathode. The cathode slurry was prepared by using 75 wt% of active material LiFePO$_4$ (LFP, Hydro-Québec), 15 wt% Conductive Carbon (Timcal-Imerys, ENSACO 350P), and 10 wt% binder (polyvinylidene fluoride, PVdF). The solid content of the slurry was maintained in the range of 26–28 wt%. LFP and Carbon were mixed in zirconia jars by a planetary ball mill
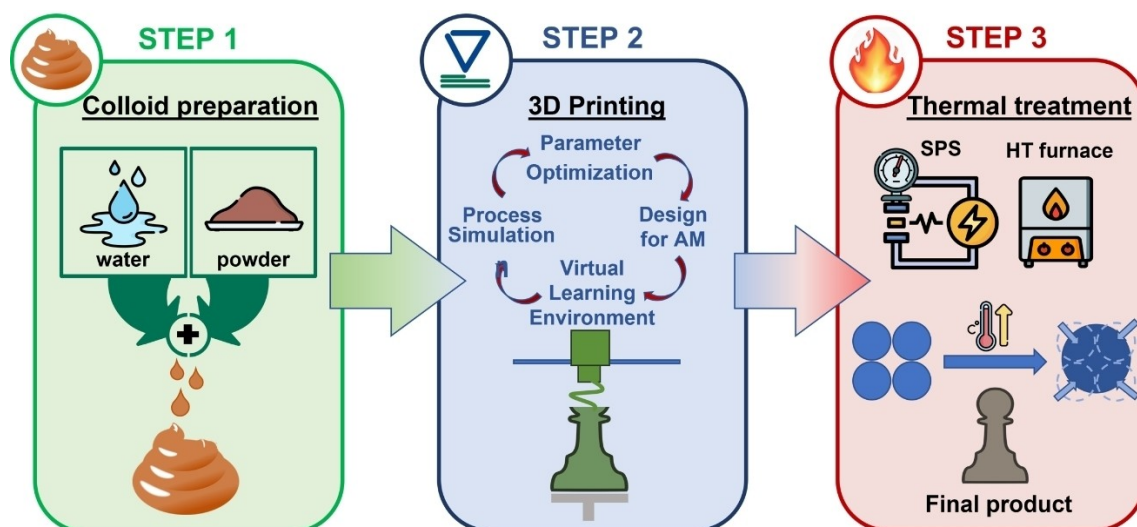

Figure 10. Schematic representation of the Cu current collector manufacturing.

Batteries & Supercaps

Research Article
doi.org/10.1002/batt.202300202

Chemistry Europe
European Chemical
Societies Publishing

at 150 rpm for 10 min, followed by a 5 min break and another 10 min milling in the reverse direction. Subsequently, it was dispersed in a solution of PVdF in N-methylpyrrolidone (NMP, Sigma-Aldrich) to obtain the slurry, which was cast on a carbon-coated aluminum foil using a doctor blade with 300 μm wet thickness. The cathode was dried under vacuum at 80 °C, cut into 2 cm^2 disks, with an active material density of 1.2 mg cm^{-2}, and stored in a glove box (MBraum, O$_2$, H$_2$O < 0.5 ppm) before the electrochemical measurements. The electrolyte was a solution of 1 M LiPF$_6$ in Ethylene Carbonate: Dimethyl Carbonate (LP30, EC: DMC, 50:50 vol.%) (Sigma-Aldrich) supported by a *Whatman* glass fiber separator. The LFP|Li@3DCu full cells were cycled on a Biologic BCS 810 battery tester in the voltage range 3–4.3 V. All the potentials reported refer to the Li$^+$/Li couple. The cell impedance was measured using EIS at room temperature by applying an AC voltage of 50 mV in the frequency range of 0.1 Hz to 1 MHz.

Acknowledgements

Conflict of Interests

The authors declare no conflict of interest.

Data Availability Statement

Research data are not shared.

[1] J. E. T. Bistline, *Joule* **2021**, *5*, 2551–2563.
[2] M. Catenacci, E. Verdolini, V. Bosetti, G. Fiorese, *Energy Policy* **2013**, *61*, 403–413.
[3] P. G. Bruce, S. A. Freunberger, L. J. Hardwick, J.-M. Tarascon, *Nat. Mater.* **2012**, *11*, 19–29.
[4] W. Weng, J. Lin, Y. Du, X. Ge, X. Zhou, J. Bao, *J. Mater. Chem. A* **2018**, *6*, 10168–10175.
[5] X.-B. Cheng, R. Zhang, C.-Z. Zhao, Q. Zhang, *Chem. Rev.* **2017**, *117*, 10403–10473.
[6] D. Koo, S. Ha, D.-M. Kim, K. T. Lee, *Curr. Opin. Electrochem.* **2017**, *6*, 70–76.
[7] C. Brissot, M. Rosso, J.-N. Chazalviel, P. Baudry, S. Lascaud, *Electrochim. Acta* **1998**, *43*, 1569–1574.
[8] D. Lin, Y. Liy, Y. Cui, *Nat. Nanotechnol.* **2017**, *12*, 194–206.
[9] Q. Zhao, X. Chen, W. Hou, B. Ye, Y. Zhang, X. Xia, J. Wang, *SusMat.* **2022**; *2*, 104–112.
[10] Y. Yang, L. Ai, J. He, C. Zhang, D. Chen, *L. Shen. Chem. Commun.* **2023**, *59*, 936–939.
[11] S. Luo, K. Pei, *IntechOpen* **2022**, *3*.
[12] X. Ma, Z. Liu, H. Chen, *Nano Energy* **2019**, *59*, 500–507.
[13] Q. Yun, Y. B. He, W. Lv, Y. Zhao, B. Li, F. Kang, Q. H. Yang, *Adv. Mater.* **2016**, *28*, 6932–6939.
[14] S. H. Wang, Y. X. Yin, T. T. Zuo, W. Dong, J. Y. Li, J. L. Shi, C. H. Zhang, N. W. Li, C. J. Li, Y. G. Guo, *Adv. Mater.* **2017**, *29*, 1703729.
[15] C.-P. Yang, Y.-X. Yin, S.-F. Zhang, N.-W. Li, Y.-G. Guo, *Nat. Commun.* **2015**, *6*, 8058.
[16] R. Song, B. Wang, Y. Xie, T. Ruan, F. Wang, Y. Yuan, D. Wang, S. Dou, *J. Mater. Chem. A* **2018**, *6*, 17967–17976.
[17] U. Gulzar, C. Glynn, C. O'Dwyer, *Curr. Opin. Electrochem.* **2020**, *20*, 46–53.
[18] L. Airoldi, U. Anselmi-Tamburini, B. Vigani, S. Rossi, P. Mustarelli, E. Quartarone, *Batteries & Supercaps* **2020**, *3*, 1040.
[19] J. Ma, S. Zheng, F. Zhou, Y. Zhu, P. Das, R. Huang, L. Zhang, X. Wang, H. Wang, Y. Cui, Z.-S. Wu. *Energy Stor. Mater* **2023**, *54*, 304–312.
[20] C. Chen, S. Li, P. H. L. Notten, Y. Zhang, Q. Hao, X. Zhang, W. Lei, *ACS Appl. Mater. Interfaces* **2021**, *13*, 24785–24794.
[21] D. Zhang, A. Dai, B. Fan, Y. Li, K. Shen, T. Xiao, G. Hou, H. Cao, X. Tao, Y. Tang, *ACS Appl. Mater. Interfaces* **2020**, *12*, 31542–31551.
[22] Y. Yang, W. Yuan, X. Zhang, Y. Ke, Z. Qiu, J. Luo, Y. Tang, C. Wang, Y. Yuan, Y. Huang, *Appl. Energy* **2020**, *276*, 115464.
[23] J.-Y. Eom, S. H. Choi, J.-H. Kang, G. H. Eom, J. Moon, M.-S. Park, *ACS Appl. Energ. Mater.* **2021**, *4*, 1936–1941.
[24] J. Wang, Q. Sun, X. Gao, C. Wang, W. Li, F. B. Holness, M. Zheng, R. Li, A. D. Price, X. Sun, T.-K. Sham, X. Sun, *ACS Appl. Mater. Interfaces* **2018**, *10*, 39794–39801.
[25] G. J. H. Lim, Z. Lyu, X. Zhang, J. J. Koh, Y. Zhang, C. He, S. Adams, J. Wang, J. Ding, *J. Mater. Chem. A* **2020**, *8*, 9058–9067.
[26] . He, L. Ai, T. Yao, Z. Xu, D. Chen, X. Zhang, L. Shen, *Energy Environ. Mater.* **2023**, e12614.
[27] T. Jang, J.-H. Kang, S. Kim, M. Shim, J. Lee, J. Song, W. Kim, K. Ryu, H. R. Byon, *ACS Appl. Energy Mater.* **2021**, *4*, 2644–2651.
[28] Y. Yang, L. Ai, S. Yu, J. He, T. Xu, D. Chen, L. Shen, *ACS Appl. Energy Mater.* **2022**, *5*, 15666–15672.
[29] L.-L. Lu, J. Ge, J.-N. Yang, S.-M. Chen, H.-B. Yao, F. Zhou, S.-H. Yu, *Nano Lett.* **2016**, *16*, 4431–4437.
[30] L. Airoldi, R. Brucculeri, P. Baldini, F. Pini, B. Vigani, S. Rossi, F. Auricchio, U. Anselmi-Tamburini, S. Morganti, *3D Print. Addit. Manuf.* **2023**, *10*, 559–568.